J. Fluid Mech. (2022), *vol*. 947, A40, doi:10.1017/jfm.2022.685

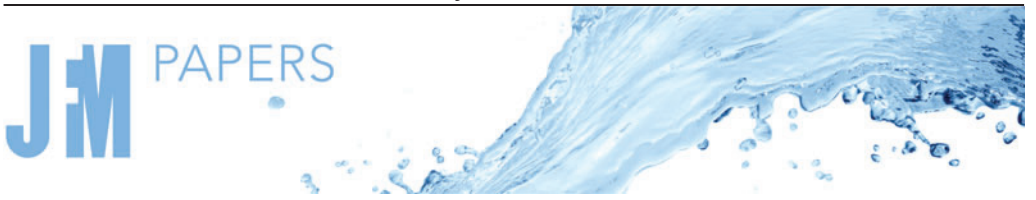

Finite-amplitude instability of the buoyancy boundary layer in a thermally stratified medium

Yue Xiao[1], **Yi Li**[1], **Moli Zhao**[1] **and Shaowei Wang**[1],†

[1]Department of Engineering Mechanics, School of Civil Engineering, Shandong University, Jinan 250061, PR China

(Received 28 May 2022; revised 29 July 2022; accepted 2 August 2022)

The finite-amplitude instability of the buoyancy-driven boundary layer is considered on a vertical plate immersed in a thermally stratified ambient medium, where the wall and surrounding fluid have different temperature gradients. Although the linear stability in this configuration has been investigated, the finite-amplitude solution arising from the critical instability has been studied only for specific parameter values. We extend this by using the amplitude expansion method. The primary bifurcations to the two-dimensional least unstable mode for different temperature gradient ratios ($0 \leqslant \lambda \leqslant 10$) and Prandtl numbers ($10^{-1} \leqslant Pr \leqslant 10^4$) are investigated. Only supercritical bifurcations are found to occur when $0 \leqslant \lambda < 2$ and $Pr \leqslant 2800$, while subcritical bifurcations are also found for larger values of temperature gradient ratio and Prandtl number. Analysis of the contribution of the nonlinear terms in the Landau coefficient reveals that the interaction of the modification of the mean flow and second harmonic for velocity with the fundamental mode for temperature plays an important role in subcritical bifurcation. Based on the Landau equation, the threshold amplitude of the nonlinear equilibrium solution is discussed as well. These encouraging results should be helpful for understanding such a buoyancy-driven flow system.

Key words: stratified flows, buoyancy-driven instability, nonlinear instability

1. Introduction

Natural convection flows can occur when a heated vertical or inclined plate is immersed in a thermally stratified ambient fluid. Such buoyancy-induced flows are very common in several industrial processes and in nature. The buoyancy-driven boundary layer representing a balance between buoyancy and viscous force is also known as the 'buoyancy layer'. For an inclined buoyancy layer, Prandtl (1952) first introduced this model to simulate the flows over valleys and mountains in stratified air. The ambient fluid was

† Email address for correspondence: shaoweiwang@sdu.edu.cn

assumed to be linearly stratified and kept a constant horizontal temperature difference with the wall. By assuming a homogeneous boundary layer, a plane parallel flow solution with temperature defect and flow reversal was derived. Relevant meteorological literature mainly focuses on diurnal/seasonal variation and the impact of actual terrain on valley wind; see the summary in Stull (1989).

Motivated by the above configuration, Prandtl's model has become a paradigm for such a buoyancy-driven flow system. Gill (1966) studied the two-dimensional convective motion in a heated rectangular cavity to simulate the vertical buoyancy layers, in which the wall and the ambient fluid have the same linear temperature gradients. The exact solution revealed that the corresponding flow is parallel and simply one-dimensional for both velocity and temperature fields. Based on this solution, the stability of a vertical buoyancy layer was analysed by Gill & Davey (1969). They obtained the neutral stability conditions for a wide range of Prandtl numbers. Iyer (1973) studied the inclined buoyancy layer solution based on linear stability analysis, and calculated the neutral curve under different inclination angles. Both transverse travelling Tolmien–Schlichting (T–S) waves and longitudinal rolls were considered. Jaluria & Gebhart (1974) investigated the effect of a stable ambient thermal stratification on the vertical boundary layer theoretically and experimentally. They assumed that the temperature difference between the vertical wall and the extensive medium varied downstream with a power law $x^{0.2}$, which guaranteed that the wall will dissipate a uniform heat flux. The results suggested that a stable ambient stratification delays the early stages of transition. Later, the finite-difference method was used to verify numerically the velocity and temperature fields by Jaluria & Himasekhar (1983). A similarity solution was obtained for the natural convection flow on an isothermal heated plate by Kulkarni, Jacobs & Hwang (1987). Based on this solution, Krizhevsky, Cohen & Tanny (1996) investigated the convective and absolute instabilities through linear instability analysis. Substantial progress has been made in many theoretical and numerical studies of Prandtl buoyancy layers (Desrayaud 1990; Gebhart *et al.* 1993; Tao, LeQuéré & Xin 2004*a*; McBain, Armfield & Desrayaud 2007; Xiong & Tao 2017). It is worth mentioning that Tao, LeQuéré & Xin (2004*b*) studied the spatio-temporal instability of the boundary layer adjacent to a vertical heated plate, in which the temperature distribution of ambient medium and wall has different linear temperature gradients. They introduced a temperature gradient ratio to describe the flow evolution for different boundary conditions in a smooth way. Besides, according to three-dimensional stability analysis (Tao & Busse 2009), the oblique roll mode is found to be more unstable than the transverse T–S wave mode at some inclination angles and Prandtl numbers due to ambient thermal stratification. Candelier, LeDizès & Millet (2012) investigated the three-dimensional stability of boundary layer flow stably stratified within an inviscid framework, and the compressible and non-Boussinesq effects on the stability properties were considered in the strongly stratified limit. Then, Chen, Bai & LeDizès (2016) found the boundary layer flow to be unstable with respect to two instabilities (i.e. viscous instability and radiative instability). And the radiative instability was shown to exhibit a much larger growth rate than the viscous instability in a large Froude-number interval with large Reynolds numbers. Parente *et al.* (2020) considered the modal and non-modal linear stability of a stably stratified Blasius boundary layer flow. The influences of Richardson, Reynolds and Prandtl numbers on the temporal and spatial linear stability were discussed. More recently, Xiao *et al.* (2022) investigated the critical and spatio-temporal instability of the buoyancy-driven boundary layer on a vertical cylinder. The results are consistent with those of a vertical plate when the radius is large enough.

In all the above-mentioned studies, the authors mainly focused on linear instability analysis, which only gives the initial growth of the infinitesimal perturbation. Linear theory fails to provide more information, such as the evolution of the perturbed flow in the first stages and the local bifurcation behaviour. Therefore, the weakly nonlinear theory is necessary to understand these problems accurately. Iyer & Kelly (1978) studied the nonlinear stability of an inclined buoyancy layer with a uniform-heat-flux wall, while only supercritical finite-amplitude wave solutions were obtained. Mizushima & Gotoh (1983) studied the nonlinear evolution of the disturbance in natural convection induced in the fluid layer between two parallel vertical walls with different temperatures. Jeschke & Beer (2001) investigated the nonlinear growth of longitudinal vortices and the development of secondary instabilities of natural convection flow in a laminar boundary layer on an inclined flat plate with a constant-heat-flux surface. The stability of buoyancy-driven convection between vertical concentric cylinders with a uniform temperature gap was also studied under vertical thermal stratification conditions (Prud'homme & LeQuéré 2007). The Landau coefficient reveals that bifurcation can be subcritical or supercritical. Wu & Zhang (2008) considered the linear and nonlinear instabilities of modified T–S waves in a stratified boundary layer. The effect of stratification on the temporal and spatial linear growth rates was studied, and the nonlinear evolution of the disturbances is related to an extension of the well-known Benjamin–Davis–Ono equation. The weakly nonlinear stability of stably stratified non-isothermal Poiseuille flow in a vertical channel was considered by Khandelwal & Bera (2015). The results show that only supercritical instability exists, which is consistent with the conclusion based on direct numerical simulation (Chen & Chung 2002, 2003).

Up to now, there has been little research on nonlinear analysis of the buoyancy layer on a vertical plate in a stratified medium. More importantly, it is still unknown how the Prandtl number and temperature gradients affect the finite-amplitude instabilities in such a system, which is the main motivation of this paper. Weakly nonlinear analysis focuses on the amplitude equation (Landau equation) and the value of the Landau coefficient. The perturbation technique used here was first developed in the work of Stuart (1958, 1960) and Watson (1960). Later, Reynolds & Potter (1967) extended and modified the method of Stuart and Watson, and applied it to shear flows. We follow the physical model developed by Tao *et al.* (2004*b*) and the amplitude expansion method formalized by Reynolds & Potter (1967). The remainder of this investigation is outlined as follows. In § 2 the governing equations of the fluid problem and the expansion formalism of weakly nonlinear stability analysis are described. The basic flow and the critical linear instability are documented in § 3. The results of nonlinear solutions and the related Landau coefficients are obtained in § 4. Finally, conclusions are presented in § 5.

2. Mathematical formulation

2.1. *Governing equations*

The two-dimensional vertical boundary layer induced by buoyancy in a stratified fluid is studied. A sketch of the geometry and the reference frame is shown in figure 1, where the streamwise coordinate x^* is measured vertically and opposite to the direction of gravitational acceleration $\boldsymbol{g}$ and y^* is the coordinate in the wall-normal direction. The heated wall temperature is assumed to vary linearly in the streamwise direction with a temperature gradient $N_w \geqslant 0$. The temperature of surrounding fluid increases independently and linearly with a gradient $N_\infty > 0$. The temperature profiles on the wall

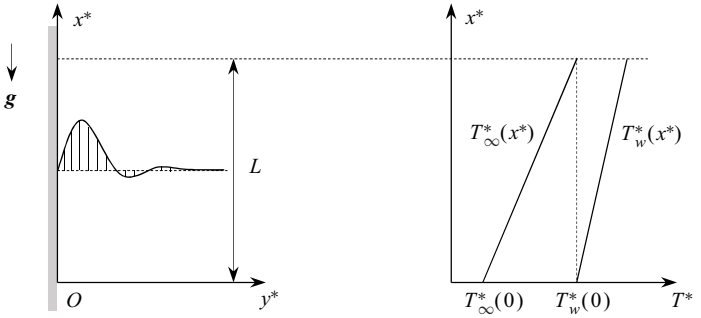

Figure 1. Schematic geometry of a vertical plate immersed in thermally stratified fluid and the temperature profiles on the wall and in the ambient medium.

and in the ambient fluid are given by

$$T_w^*(x) = T_w^*(0) + N_w x^*, \quad T_\infty^*(x) = T_\infty^*(0) + N_\infty x^*, \quad T_w^*(0) - T_\infty^*(0) > 0, \quad (2.1a\text{–}c)$$

where the subscript '∞' and the superscript '$*$' denote the ambient condition and dimensional quantities, respectively.

The heated wall is assumed to be of finite extent, and its temperature is greater than that of the surrounding fluid at any elevation. The temperature difference between the wall and the surrounding fluid at $x^* = 0$ is $\Delta T^* = T_w^*(0) - T_\infty^*(0)$. Length L is the characteristic length scale satisfying $T_w^*(0) = T_\infty^*(L)$, as shown in figure 1 by the vertical dashed line. The governing equations for continuity, momentum and energy are

$$\nabla \cdot \boldsymbol{u}^* = 0, \quad (2.2a)$$

$$\frac{\partial \boldsymbol{u}^*}{\partial t^*} + \boldsymbol{u}^* \cdot \nabla \boldsymbol{u}^* = -\nabla(P^*/\rho_r) - \boldsymbol{g}\beta(T^* - T_\infty^*) + \nu \nabla^2 \boldsymbol{u}^*, \quad (2.2b)$$

$$\frac{\partial T^*}{\partial t^*} + \boldsymbol{u}^* \cdot \nabla T^* = \kappa \nabla^2 T^*, \quad (2.2c)$$

where ρ_r is a reference density, β the coefficient of thermal expansion, ν the kinematic viscosity and κ the thermal diffusivity.

Following the non-dimensional variables employed by Tao *et al.* (2004*b*),

$$\left.\begin{aligned} \lambda = \frac{N_w}{N_\infty}, \quad Gr = \left(\frac{g\beta\Delta T^* L^3}{\nu^2}\right)^{1/4}, \quad Pr = \frac{\nu}{\kappa}, \quad t = t^* \frac{\nu Gr^3}{L^2}, \quad (x, y) = (x^*, y^*)\frac{Gr}{L}, \\ (u, v) = (u^*, v^*)\frac{L}{\nu\, Gr^2}, \quad T = \frac{T^* - T_\infty^*(x^*)}{T_w^*(x^*) - T_\infty^*(x^*)}, \quad P = \frac{P^* - P_\infty^*(x^*)}{\rho \nu^2 Gr^4} L^2, \end{aligned}\right\} \quad (2.3)$$

where λ is the temperature gradient ratio, Gr the Grashof number and Pr the Prandtl number. Note that the definition of the Grashof number used here differs from the conventional definition by 1/4 power. When the wall is isothermally heated ($N_w = 0$), we have $\lambda = 0$ for the isothermal boundary condition. And the unit temperature gradient ratio represents a uniform-heat-flux boundary condition. Let $\varepsilon = 1/Gr$ characterize the degree of spatial inhomogeneity of the basic flow. Making the standard Boussinesq approximations, the dimensionless governing equations for the velocity and temperature

according to these scaling are then

$$\frac{\partial u}{\partial x}+\frac{\partial v}{\partial y}=0, \tag{2.4a}$$

$$\frac{\partial u}{\partial t}+u\frac{\partial u}{\partial x}+v\frac{\partial u}{\partial y}=-\frac{\partial P}{\partial x}+\frac{1}{Gr}\nabla^2 u+\frac{1}{Gr}T[1+(\lambda-1)\varepsilon x], \tag{2.4b}$$

$$\frac{\partial v}{\partial t}+u\frac{\partial v}{\partial x}+v\frac{\partial v}{\partial y}=-\frac{\partial P}{\partial y}+\frac{1}{Gr}\nabla^2 v, \tag{2.4c}$$

$$\frac{\partial T}{\partial t}+u\frac{\partial T}{\partial x}+v\frac{\partial T}{\partial y}=\frac{1}{Pr\,Gr}\nabla^2 T-\frac{u[1+(\lambda-1)T]}{Gr[1+(\lambda-1)\varepsilon x]}+\frac{2(\lambda-1)}{Pr}\frac{\partial T}{\partial x}\varepsilon^2, \tag{2.4d}$$

with the boundary conditions

$$u(t,x,0)=v(t,x,0)=u(t,x,\infty)=T(t,x,\infty)=0,\quad T(t,x,0)=1. \tag{2.5a,b}$$

In the linearized analysis, the perturbations of velocity and temperature are assumed as $\Gamma(y)\exp[\mathrm{i}(\tilde{\alpha}x+\omega t)]\exp(at)$, where $\tilde{\alpha}$ represents the streamwise wavenumber and $\omega-\mathrm{i}a$ would emerge as the complex eigenvalue in the linear problem. Parameters ω and a are the frequency and growth rate of the basic wave, respectively. In the nonlinear analysis, we seek solutions in terms of the basic wave and its harmonics, and the following initial transformations of variables are utilized:

$$\theta=\tilde{\alpha}x+\tilde{\omega}t,\quad \tilde{\omega}=\tilde{\omega}(A),\quad A=A(t). \tag{2.6a–c}$$

Note that $A(t)$ is the amplitude of the fluctuations and the frequency also depends upon the amplitude. Considering the new variables (2.6*a–c*), the continuity in (2.4) is automatically satisfied by introducing a stream function $\psi(\theta,A,y)$, such that

$$\frac{\partial\psi}{\partial y}=\tilde{\alpha}u,\quad \frac{\partial\psi}{\partial\theta}=-v. \tag{2.7a,b}$$

Substituting (2.6*a–c*) and (2.7*a,b*) into (2.4), then eliminating the pressure P, we obtain the equations for ψ and T:

$$\frac{\mathrm{d}A}{\mathrm{d}t}\frac{\partial\zeta}{\partial A}+\left[\tilde{\omega}+\frac{\mathrm{d}\tilde{\omega}}{\mathrm{d}A}\left(t\frac{\mathrm{d}A}{\mathrm{d}t}\right)\right]\frac{\partial\zeta}{\partial\theta}+J(\psi,\zeta)=\frac{1}{Gr}\nabla_{\tilde{\alpha}}^2\zeta+\frac{\tilde{\alpha}f(x)}{2\sqrt{2}\,Gr}\frac{\partial T}{\partial y}, \tag{2.8a}$$

$$\frac{\mathrm{d}A}{\mathrm{d}t}\frac{\partial T}{\partial A}+\left[\tilde{\omega}+\frac{\mathrm{d}\tilde{\omega}}{\mathrm{d}A}\left(t\frac{\mathrm{d}A}{\mathrm{d}t}\right)\right]\frac{\partial T}{\partial\theta}+J(\psi,T)=\frac{1}{Pr\,Gr}\nabla_{\tilde{\alpha}}^2 T-\frac{2\sqrt{2}[1+(\lambda-1)T]}{Gr\,\tilde{\alpha}f(x)}\frac{\partial\psi}{\partial y}+O(\varepsilon^2), \tag{2.8b}$$

where $\zeta=\nabla_{\tilde{\alpha}}^2\psi$, $J(f,g)$ is the Jacobian determinant defined by $(\partial f/\partial y)(\partial g/\partial\theta)-(\partial f/\partial\theta)(\partial g/\partial y)$, $\nabla_{\tilde{\alpha}}^2=\partial^2/\partial y^2+\tilde{\alpha}^2\partial^2/\partial\theta^2$ and $f(x)=2\sqrt{2}[1+(\lambda-1)\varepsilon x]$. The corresponding boundary conditions are

$$\psi(\theta,A,0)=\frac{\partial\psi}{\partial y}(\theta,A,0)=\frac{\partial\psi}{\partial\theta}(\theta,A,0)=0,\quad T(\theta,A,0)=1, \tag{2.9a}$$

$$\frac{\partial\psi}{\partial y}(\theta,A,\infty)=0,\quad T(\theta,A,\infty)=0. \tag{2.9b}$$

2.2. *The expansion formalism*

In order to simplify the equations, the modified Grashof number G, wavenumber α and frequency ω are introduced:

$$G = f(x)Gr, \quad \alpha = \sqrt{2}\tilde{\alpha}, \quad \omega = \frac{2}{f(x)}\tilde{\omega}, \quad \tau = \frac{f(x)}{2}t, \quad \eta = \frac{y}{\sqrt{2}}. \tag{2.10a–e}$$

Then, we expand the stream function and temperature in terms of their harmonic component:

$$\psi(\theta, A, \eta) = f(\theta)\sum_{k=0}^{\infty}[\Psi^{(k)}(A, \eta)\exp(\mathrm{i}k\theta) + \overline{\Psi^{(k)}}(A, \eta)\exp(-\mathrm{i}k\theta)], \tag{2.11a}$$

$$T(\theta, A, \eta) = \sum_{k=0}^{\infty}\Theta^{(k)}(A, \eta)\exp(\mathrm{i}k\theta) + \overline{\Theta^{(k)}}(A, \eta)\exp(-\mathrm{i}k\theta), \tag{2.11b}$$

where the overline denotes a complex conjugate. For a small-amplitude disturbance, the perturbed flow can be expanded around the basic flow. Thus, the solutions will be expanded as a power series in the amplitude A:

$$\Psi^{(k)}(A, \eta) = \sum_{n=k}^{\infty}A^n\phi^{(k,n)}(\eta), \quad \Theta^{(k)}(A, \eta) = \sum_{n=k}^{\infty}A^n\varphi^{(k,n)}(\eta). \tag{2.12a,b}$$

In the dual superscript notation, the first index (k) refers to a particular Fourier mode and the second index (n) indicates the order of a particular term as $O(A^n)$. These forms of solutions can be reduced to the basic laminar flow with $O(1)$ terms and linear problem with $O(A)$ terms. Equation (2.12*a*,*b*) represents the sum over all $n \geqslant k$, so $\Psi^{(k)}$ contains no terms of order less than A^k. Following the series expansion forms utilized by Reynolds & Potter (1967), the term $\mathrm{d}A/\mathrm{d}\tau$ and the term involving ω are represented by power series in A:

$$\frac{1}{A}\frac{\mathrm{d}A}{\mathrm{d}\tau} = \sum_{n=0}^{\infty}A^n a^{(n)}, \quad \omega + \frac{\mathrm{d}\omega}{\mathrm{d}A}\left(\tau\frac{\mathrm{d}A}{\mathrm{d}\tau}\right) = \sum_{n=0}^{\infty}A^n b^{(n)}. \tag{2.13a,b}$$

For linear stability analysis, $a^{(0)}$ and $b^{(0)}$ emerge as the eigenvalues. Terms $a^{(1)}$ and $b^{(1)}$ will turn out to be zero. Term $a^{(2)}$ may moderate or accelerate the exponential growth of the linear disturbance, which is the focus of interest in nonlinear analysis. According to the signs of $a^{(0)}$ and $a^{(2)}$, one can determine whether the primary bifurcation is supercritical or subcritical. The equation for the slowly varying amplitude $A(\tau)$ is also known as the Landau equation and the coefficients are referred to as Landau coefficients.

Substituting (2.11)–(2.13*a*,*b*) into (2.8) and collecting like terms with different order, a set of coupled ordinary differential equations for $\phi^{(k,n)}(\eta)$ and $\varphi^{(k,n)}(\eta)$ will be obtained, and the equations can be solved sequentially. The governing equations and corresponding boundary conditions for $\phi^{(k,n)}(\eta)$ and $\varphi^{(k,n)}(\eta)$ are given in Appendix A. Equation (A1) with corresponding boundary conditions embody all necessary information for the nonlinear analysis of the buoyancy-driven flow. In a later section, we reduce the nonlinear stability problem to a sequence of linear homogeneous/inhomogeneous differential equations for $\phi^{(k,n)}(\eta)$ and $\varphi^{(k,n)}(\eta)$, each of which can be solved numerically. Additionally, according to the discussion by Reynolds & Potter (1967), $a^{(n)}$ and $b^{(n)}$ for odd

$\phi^{(0,0)}$	—	—	—	$\varphi^{(0,0)}$	—	—	—
—	$\phi^{(1,1)}$	—	—	—	$\varphi^{(1,1)}$	—	—
$\phi^{(0,2)}$	—	$\phi^{(2,2)}$	—	$\varphi^{(0,2)}$	—	$\varphi^{(2,2)}$	—
—	$\phi^{(1,3)}$	—	$\phi^{(3,3)}$	—	$\varphi^{(1,3)}$	—	$\varphi^{(3,3)}$
...	—	—	—	...	—	—	—

Table 1. Non-zero functions for $\phi^{(k,n)}$ and $\varphi^{(k,n)}$ for $k \leqslant n$.

n vanish. Besides, the functions $\phi^{(k,n)}$ and $\varphi^{(k,n)}$ also vanish if $n + k$ is odd. The calculation in this paper also confirms this result, and hence the remaining non-zero functions (see table 1) are discussed in the following.

3. Linear stability analysis

To predict the stability in our framework, we start by performing the linear stability analysis of the basic state $\phi^{(0,0)}$ and $\varphi^{(0,0)}$, which was previously done by Tao *et al.* (2004*b*). We briefly rederive their results in the following subsection so that they can be applied in the later weakly nonlinear analysis.

3.1. *Basic flow* ($k = 0, n = 0$)

For the steady and spatial inhomogeneous base flow, it is necessary to take $k = 0$ and $n = 0$ into (A1). Then we obtain

$$\mathscr{D}^4\phi^{(0,0)} + \frac{8\sqrt{2}(\lambda-1)}{\alpha}(\phi^{(0,0)}\mathscr{D}^3\phi^{(0,0)} - \mathscr{D}\phi^{(0,0)}\mathscr{D}^2\phi^{(0,0)}) + \frac{\alpha}{\sqrt{2}}\mathscr{D}\varphi^{(0,0)} = 0, \tag{3.1a}$$

$$\frac{1}{Pr}\mathscr{D}^2\varphi^{(0,0)} - \frac{4\sqrt{2}}{\alpha}\mathscr{D}\phi^{(0,0)}[1 + 2(\lambda-1)\varphi^{(0,0)}] + \frac{8\sqrt{2}(\lambda-1)}{\alpha}\phi^{(0,0)}\mathscr{D}\varphi^{(0,0)} = 0, \tag{3.1b}$$

where $\mathscr{D} = \mathrm{d}/\mathrm{d}\eta$. Because we used the transformation (2.6*a–c*) before, the wavenumber α appears as a coefficient in (3.1). However, the basic flow is independent of the wavenumber. We change the above equations into a more reasonable form by transforming $F_0 = 2\sqrt{2}\alpha^{-1}\phi^{(0,0)}$ and $H_0 = 2\varphi^{(0,0)}$. The following equations are obtained, which are consistent with those of Tao *et al.* (2004*b*). For the sake of simplicity, the derivative of the basic flow with respect to η is represented by a prime:

$$F_0''' + 4(\lambda-1)\left(F_0F_0''' - F_0'F_0''\right) + H_0 = 0, \tag{3.2a}$$

$$Pr^{-1}H_0'' + 4(\lambda-1)F_0H_0' - 4F_0'[1 + (\lambda-1)H_0] = 0, \tag{3.2b}$$

with boundary conditions

$$F_0(0) = F_0'(0) = F_0'(\infty) = H_0(\infty) = 0, \quad H_0(0) = 1. \tag{3.3a,b}$$

In order to solve the ordinary equations (3.2), we regard this problem as a two-point boundary value problem. The coupled equations are first transformed into a system of five first-order differential equations. Then, after a coordinate transformation, the

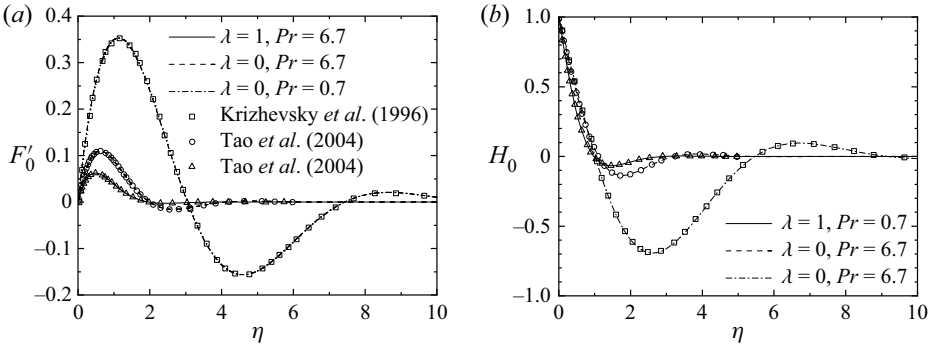

Figure 2. Comparison of basic flow (*a*) $F_0'(\eta)$ and (*b*) $H_0(\eta)$ profiles between the present results (lines) and previous results (symbols) for different λ and Pr. Solid lines (triangle), $\lambda = 1$, $Pr = 6.7$; dashed lines (circle), $\lambda = 0$, $Pr = 6.7$; dash-dotted lines (square), $\lambda = 0$, $Pr = 0.7$.

Gauss–Lobatto points are adopted to discretize the system of differential equations in the η interval $[0, \eta_{max}]$. The solution obtained by Prandtl (1952) for a one-dimensional flow is taken as the initial guess for the Newton iterations. For a high enough numerical accuracy, the order of Chebyshev polynomial N and a large enough η_{max} must be chosen. As a consequence, the parameters are determined when the absolute value of the residual varies by less than 10^{-10} on each iteration. The numerical solutions of dimensionless vertical velocity $F_0'(\eta)$ and temperature $H_0(\eta)$ for different temperature gradient ratios and Prandtl numbers are tested successfully against the results of Krizhevsky *et al.* (1996) and Tao *et al.* (2004*b*) (see figure 2). The discussions for related velocity and temperature profiles can be found in their works and hence we do not repeat them here for the sake of brevity.

3.2. *Critical instability: fundamental mode* ($k = 1, n = 1$)

In the linear problem at $O(A)$, it is assumed that the disturbances are infinitesimal to the basic state. Substituting $k = 1$ and $n = 1$ into (A1), the Orr–Sommerfeld equation coupled with the energy equation is obtained:

$$\boldsymbol{Q}^{(1,1)}\boldsymbol{X}^{(1,1)} = (a^{(0)} + \mathrm{i}b^{(0)})\boldsymbol{S}\boldsymbol{X}^{(1,1)}, \tag{3.4}$$

where $\boldsymbol{X}^{(k,n)} = (\phi^{(k,n)}, \varphi^{(k,n)})^{\mathrm{T}}$, and $\boldsymbol{Q}^{(1,1)}$ and $\boldsymbol{S}$ are

$$\boldsymbol{Q}^{(1,1)} = \begin{pmatrix} \dfrac{1}{G}\mathscr{L}_1^2 + \mathrm{i}\alpha\left(F_0''' - F_0'\mathscr{L}_1\right) & \dfrac{\alpha}{\sqrt{2}G}\mathscr{D} \\ \mathrm{i}\sqrt{2}H_0' - \dfrac{4\sqrt{2}}{\alpha G}\left[1 + (\lambda - 1)H_0\right]\mathscr{D} & \dfrac{1}{Pr\,G}\mathscr{L}_1 - \mathrm{i}\alpha F_0' - \dfrac{4}{G}(\lambda - 1)F_0' \end{pmatrix}, \tag{3.5}$$

$$\boldsymbol{S} = \begin{pmatrix} \mathscr{L}_1 & 0 \\ 0 & 1 \end{pmatrix}, \tag{3.6}$$

with $\mathscr{L}_k = \mathscr{D}^2 - k^2\alpha^2$, and the superscript T denotes the transposition operation for a vector. The boundary conditions are

$$\phi^{(1,1)}(0) = \mathscr{D}\phi^{(1,1)}(0) = \mathscr{D}\phi^{(1,1)}(\infty) = \varphi^{(1,1)}(0) = \varphi^{(1,1)}(\infty) = 0. \tag{3.7}$$

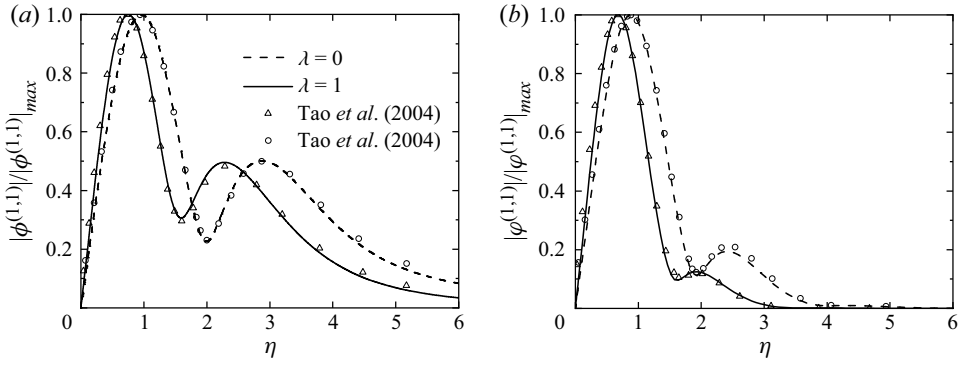

Figure 3. Comparison of amplitude profiles of critical modes between the present results (lines) and previous results (symbols) for $Pr = 6.7$. (*a*) Velocity disturbance and (*b*) temperature disturbance for $\lambda = 1$ and $\lambda = 0$.

Equations (3.4) and (3.7) constitute eigenvalue problems, which determine a set of eigenvalues of $a^{(0)}$ and $b^{(0)}$, as well as the corresponding eigenfunctions of $\phi^{(1,1)}$ and $\varphi^{(1,1)}$. The real and imaginary parts of the phase velocity $c^{(0)}$ are represented by $c_r^{(0)} = -b^{(0)}/\alpha$ and $c_i^{(0)} = a^{(0)}/\alpha$, respectively. The disturbance is neutrally stable as $c_i^{(0)} = 0$. It is worth noting that there are two more terms related to λ in (3.5) when compared with (2.8*a*) in Tao *et al.* (2004*b*), which were ignored in their work. Although these two terms have little effect on the results of linear stability analysis, they are crucial to the weak nonlinear problems in the later analysis. The amplitude profiles of critical modes, shown in figure 3 as solid line ($\lambda = 1$) and dashed line ($\lambda = 0$), agree well with the results from Tao *et al.* (2004*b*). The generalized eigenvalue problem (3.4) is then solved using a spectral eigenvalue solver based on Chebyshev polynomials. We first map the computational Chebyshev domain $[-1, 1]$ onto the physical domain $[0, \eta_{max}]$ via a linear coordinate transformation. For different parameters (e.g. Prandtl number and the temperature gradient ratio), several tests have been performed for different Chebyshev points and computational domains to ensure numerical convergence. To determine the neutral states, for given parameters of Pr and λ, α and G are varied until $|c_i^{(0)}| \leqslant 10^{-6}$. In all subsequent numerical calculations, the number of Chebyshev points $N = 200$ are used to accurately compute the generalized eigenvalue problem. For more details on numerical calculation, we refer the reader to Schmid & Henningson (2001) and Xiao *et al.* (2022).

The neutral curves of G versus α and $c_r^{(0)}$ for different Pr and λ are shown in figure 4. The neutral curves exhibit the common feature in the buoyancy-driven system, i.e. the neutral curves have higher- and lower-wavenumber parts. Those two-lobed structures (also known as the nose-shaped piece) are determined by thermal instability and mechanical instability (Gill & Davey 1969). The lower-wavenumber part is caused by the coupling between the Orr–Sommerfeld equation and the energy equation, which corresponds to buoyancy-driven instability. The higher-wavenumber part is controlled by mechanical instability, and the feature does not change when the buoyancy effects are neglected. The minimum value of Grashof number on the curve determines the critical Grashof number G_c. The corresponding wavenumber and phase velocity are denoted as α_c and $c_c^{(0)}$. With an increase of λ, the critical Grashof number G_c increases while $c_c^{(0)}$ decreases, which means a larger gradient ratio λ stabilizes the buoyancy layer. The critical parameters for different values of Pr and λ are shown in table 2. Besides, the loop of the neutral curve for $Pr = 6.7$ and $\lambda = 0$ (see figure 4*c*) is produced by the twist in the (α, G, ω) space.

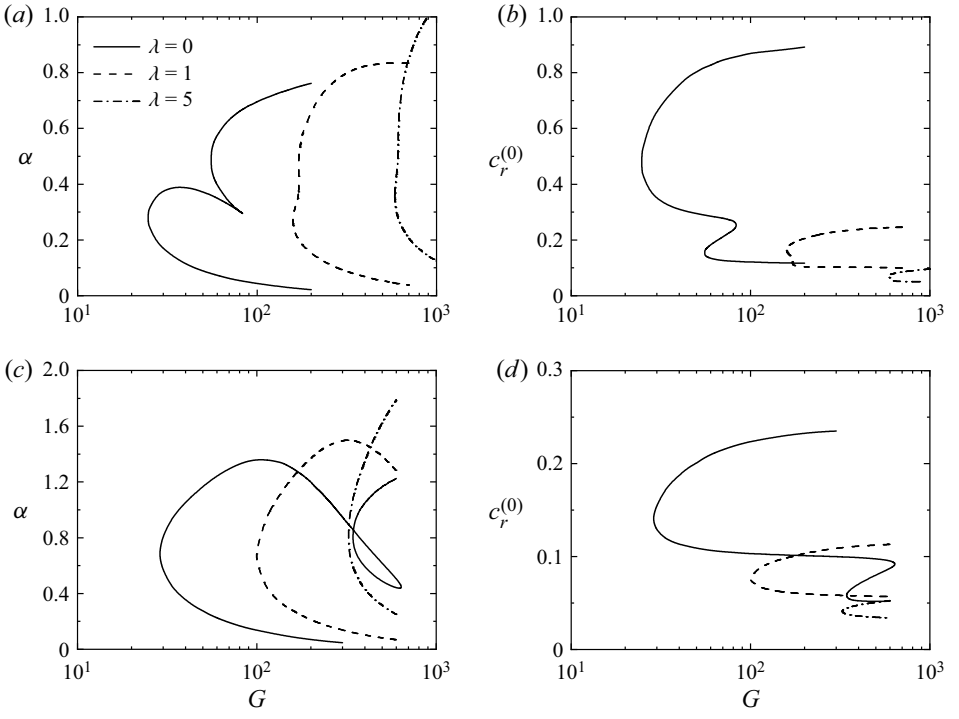

Figure 4. The neutral curves for different temperature gradient ratios λ in (a,c) (α, G) plane and (b,d) ($c_r^{(0)}$, G) plane for (a,b) $Pr = 0.72$ and (c,d) $Pr = 6.7$.

In order to fix the amplitude of $\phi^{(1,1)}$ and $\varphi^{(1,1)}$, the amplitude of the eigenfunction is normalized by

$$\langle \phi^{(1,1)}, \phi^{(1,1)} \rangle + \langle \varphi^{(1,1)}, \varphi^{(1,1)} \rangle = 1 \tag{3.8}$$

with the inner product

$$\langle f, g \rangle = \int_0^\infty \overline{f(\eta)} g(\eta)\, \mathrm{d}\eta. \tag{3.9}$$

Due to the lack of explicit expressions for the solutions to the linear problem, the inner products need to be computed numerically. The Clenshaw–Curtis quadrature (Trefethen 2008) on the Gauss–Lobatto collocation grid is applied to evaluate the integral. We will see that the following equations for the higher-order problem can be solved one by one with the known $\phi^{(1,1)}$ and $\varphi^{(1,1)}$.

4. Weakly nonlinear analysis

4.1. *Modification of the mean flow* ($k = 0, n = 2$)

For the distortion of mean flow on $O(A^2)$, substituting $k = 0$ and $n = 2$ into (A1), we have

$$\boldsymbol{Q}^{(0,2)} \boldsymbol{X}^{(0,2)} = \boldsymbol{F}^{(0,2)}, \tag{4.1}$$

where

$$\boldsymbol{Q}^{(0,2)}=\begin{pmatrix}\dfrac{1}{G}\mathscr{L}_0^2-\mathscr{M}^{(0,2)}\mathscr{L}_0 & \dfrac{\alpha}{\sqrt{2}G}\mathscr{D}\\ -\dfrac{4\sqrt{2}}{\alpha G}[1+(\lambda-1)H_0]\mathscr{D} & \dfrac{1}{PrG}\mathscr{L}_0-\mathscr{M}^{(0,2)}-\dfrac{4}{G}(\lambda-1)F_0'\end{pmatrix}, \tag{4.2}$$

$$\boldsymbol{F}^{(0,2)}=\begin{pmatrix}\dfrac{\sqrt{2}}{2}\mathrm{i}\mathscr{D}(\overline{\phi^{(1,1)}}\mathscr{L}_1\phi^{(1,1)}-\phi^{(1,1)}\mathscr{L}_1\overline{\phi^{(1,1)}})\\ \dfrac{\sqrt{2}}{2}\mathrm{i}\mathscr{D}(\overline{\phi^{(1,1)}}\varphi^{(1,1)}-\phi^{(1,1)}\overline{\varphi^{(1,1)}})\\ +\dfrac{2\sqrt{2}}{\alpha G}(\lambda-1)(\mathscr{D}\phi^{(1,1)}\overline{\varphi^{(1,1)}}+\mathscr{D}\overline{\phi^{(1,1)}}\varphi^{(1,1)})\end{pmatrix}, \tag{4.3}$$

with $\mathscr{M}^{(k,n)}=na^{(0)}+\mathrm{i}kb^{(0)}+\mathrm{i}k\alpha F_0'$. From the expression of $\boldsymbol{F}^{(0,2)}$, it suggests that the interaction of the fundamental mode with its complex conjugate leads to the distortion of mean flow. Since we have already obtained the fundamental mode, (4.1) with the associated boundary conditions is solved numerically. Furthermore, note that $\boldsymbol{Q}^{(0,2)}$ is a real matrix, i.e. $\boldsymbol{Q}^{(0,2)}=\overline{\boldsymbol{Q}^{(0,2)}}$. It is easy to prove that $\boldsymbol{X}^{(0,2)}$ is always real.

Figure 5 illustrates the modification of the mean flow for two sets of parameters: $Pr=6.7$ for different λ, and $\lambda=0$ for different Pr. For $Pr=6.7$, the position of the maximum value for the modification of the mean flow moves towards the wall at higher gradient ratio λ due to a thinner boundary layer. And the maximum value of the correction of velocity and temperature increases with an increase of λ. However, near the wall, the defect of velocity decreases with an increase of λ (figure 5*a*), which is contrary to the temperature (figure 5*b*). The modifications of the mean flow with different Pr for an isothermal wall ($\lambda=0$) are shown in figure 5(*c*,*d*). With an increase of Pr, the amount of correction increases constantly, but the position of the maximum value does not change monotonically. Nevertheless, the curves have a common feature: there is a maximum value and two minimum values. And the value of basic flow near the wall will decrease to some extent.

4.2. *Second harmonic of the fundamental* ($k=2, n=2$)

The equation for the second harmonic is derived by substituting $k=n=2$ into (A1), and we have

$$\boldsymbol{Q}^{(2,2)}\boldsymbol{X}^{(2,2)}=\boldsymbol{F}^{(2,2)}, \tag{4.4}$$

where

$$\boldsymbol{Q}^{(2,2)}=\begin{pmatrix}\dfrac{1}{G}\mathscr{L}_2^2-\mathscr{M}^{(2,2)}\mathscr{L}_2+2\mathrm{i}\alpha F_0''' & \dfrac{\alpha}{\sqrt{2}G}\mathscr{D}\\ 2\sqrt{2}\mathrm{i}H_0'-\dfrac{4\sqrt{2}}{\alpha G}[1+(\lambda-1)H_0]\mathscr{D} & \dfrac{1}{PrG}\mathscr{L}_2-\mathscr{M}^{(2,2)}-\dfrac{4}{G}(\lambda-1)F_0'\end{pmatrix}, \tag{4.5}$$

$$\boldsymbol{F}^{(2,2)}=\begin{pmatrix}\sqrt{2}\mathrm{i}(\mathscr{D}\phi^{(1,1)}\mathscr{L}_1\phi^{(1,1)}-\phi^{(1,1)}\mathscr{L}_1\mathscr{D}\phi^{(1,1)})\\ \sqrt{2}\mathrm{i}(\mathscr{D}\phi^{(1,1)}\varphi^{(1,1)}-\phi^{(1,1)}\mathscr{D}\varphi^{(1,1)})+\dfrac{4\sqrt{2}}{\alpha G}(\lambda-1)\mathscr{D}\phi^{(1,1)}\varphi^{(1,1)}\end{pmatrix}. \tag{4.6}$$

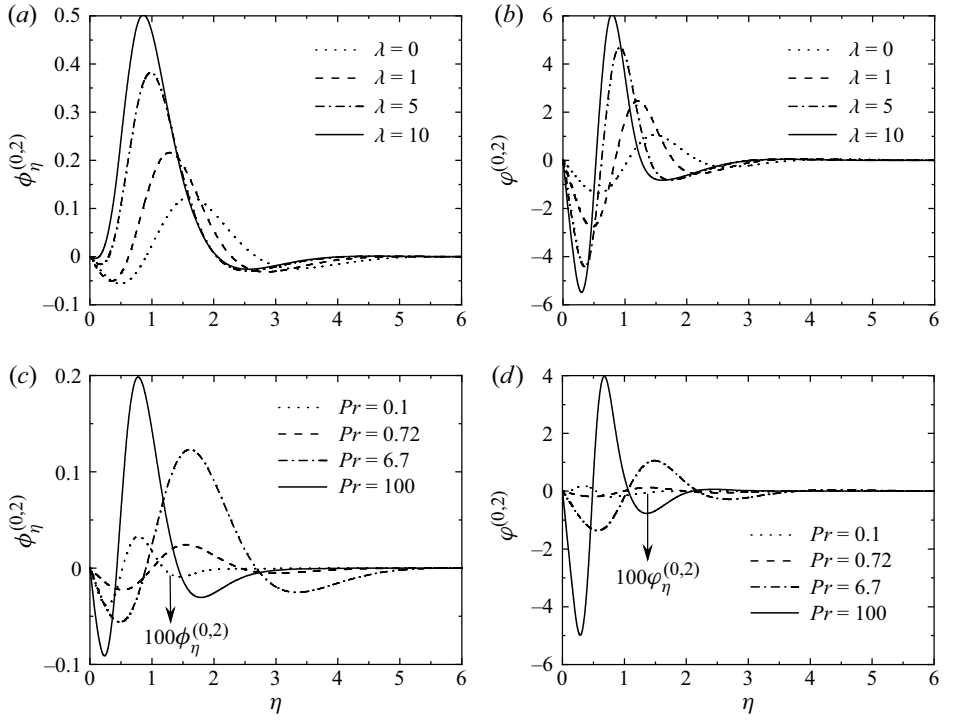

Figure 5. Modification of the mean flow. (*a*) Velocity and (*b*) temperature as functions of η for different values of λ with $Pr = 6.7$. (*c*) Velocity and (*d*) temperature as functions of η for different values of Pr with $\lambda = 0$. For the case of $Pr = 0.1$ in (*c*,*d*), the dotted lines are magnified by 100 times.

Similarly, (4.6) implies that the fundamental mode interacting with itself leads to the generation of the second harmonic. The amplitude profiles of the second harmonic of the fundamental for different Pr and λ are shown in figure 6. For given $Pr = 6.7$, it can be seen from figures 6(*a*) and 6(*b*) that the velocity curve contains three peaks, but the temperature curve only has one. And with increasing λ, all of the peaks approach the wall gradually. Compared with the linear critical mode for velocity disturbance in Tao *et al.* (2004*b*), the position of the second and third peaks of $|\phi_\eta^{(2,2)}|$ almost coincides with the extreme position of the linear mode corresponding to the buoyancy-driven instability mode. Besides, the distinction is that there will be an additional peak in the near-wall region for the velocity of the second harmonic of the fundamental, and the emergence of this peak is related to the interaction between linear modes. For $\lambda = 0$, the maximum value of each curve increases as Pr increases (see figure 6*c*,*d*). In figure 6(*c*), the amplitude profiles for $Pr = 0.72$ and 6.7 have three peaks, while for a large or small value of Pr, the profiles have only two peaks. Considering the physical meaning of the Prandtl number, the number of peaks in the second harmonic of the fundamental may be related to the competition between momentum transport and heat transport.

4.3. *Landau coefficient* ($k = 1, n = 3$)

At $O(A^3)$, we derive an equation for the distortion of the fundamental mode $\phi^{(1,3)}$ and $\varphi^{(1,3)}$ by substituting $k = 1$ and $n = 3$ into (A1):

$$\boldsymbol{Q}^{(1,3)}\boldsymbol{X}^{(1,3)} = (a^{(2)} + \mathrm{i}b^{(2)})\boldsymbol{S}\boldsymbol{X}^{(1,1)} + \boldsymbol{F}^{(1,3)}, \tag{4.7}$$

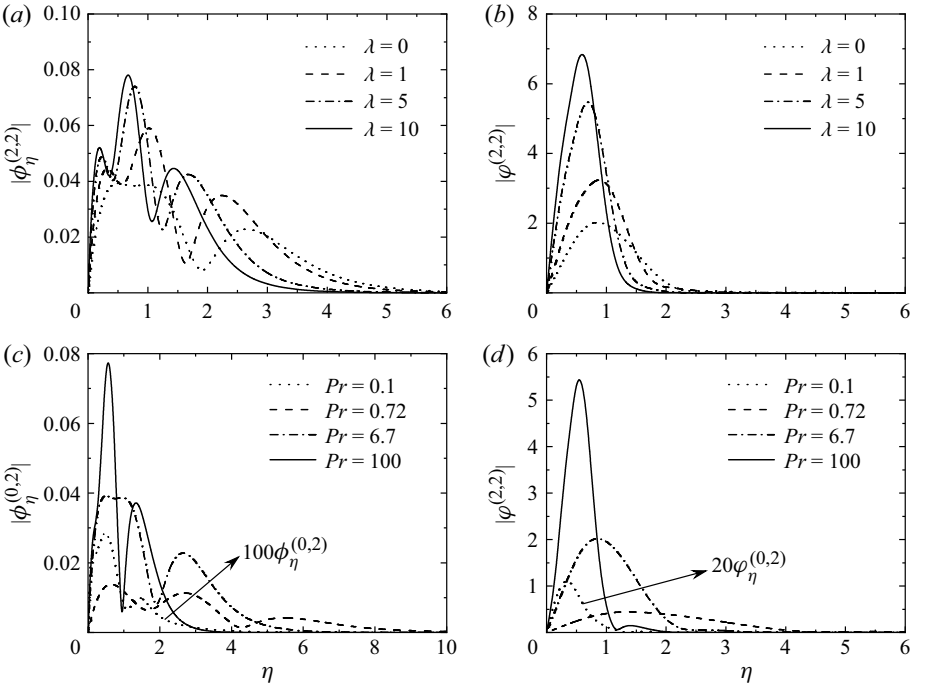

Figure 6. Amplitude profiles of the second harmonic of the fundamental. (*a*) Velocity and (*b*) temperature as functions of η for different values of λ with $Pr = 6.7$. (*c*) Velocity and (*d*) temperature as functions of η for different values of Pr with $\lambda = 0$. For the case of $Pr = 0.1$ in (*c*,*d*), the dotted lines are magnified by 100 and 20 times, respectively.

where

$$\boldsymbol{Q}^{(1,3)} = \begin{pmatrix} \dfrac{1}{G}\mathscr{L}_1^2 - \mathscr{M}^{(1,3)}\mathscr{L}_1 + \mathrm{i}\alpha F_0''' & \dfrac{\alpha}{\sqrt{2}G}\mathscr{D} \\ \sqrt{2}\mathrm{i}H_0' - \dfrac{4\sqrt{2}}{\alpha G}[1 + (\lambda - 1)H_0]\mathscr{D} & \dfrac{1}{Pr\,G}\mathscr{L}_1 - \mathscr{M}^{(1,3)} - \dfrac{4}{G}(\lambda - 1)F_0' \end{pmatrix}, \tag{4.8}$$

and the expression for the inhomogeneous term $\boldsymbol{F}^{(1,3)}$ represents the quadratic nonlinear terms that arise from the product of two Fourier series:

$$\boldsymbol{F}^{(1,3)} = \begin{pmatrix} \mathscr{N}_M^{01} + \mathscr{N}_M^{12} \\ \mathscr{N}_E^{01} + \mathscr{N}_E^{10} + \mathscr{N}_E^{12} + \mathscr{N}_E^{21} \end{pmatrix}, \tag{4.9}$$

with

$$\mathscr{N}_M^{01} = -\sqrt{2}\mathrm{i}[(\mathscr{D}\phi^{(0,2)} + \mathscr{D}\overline{\phi^{(0,2)}})\mathscr{L}_1\phi^{(1,1)} - \phi^{(1,1)}\mathscr{L}_0(\mathscr{D}\phi^{(0,2)} + \mathscr{D}\overline{\phi^{(0,2)}})], \tag{4.10a}$$

$$\mathscr{N}_M^{12} = -\sqrt{2}\mathrm{i}(2\mathscr{D}\overline{\phi^{(1,1)}}\mathscr{L}_2\phi^{(2,2)} - \mathscr{D}\phi^{(2,2)}\mathscr{L}_1\overline{\phi^{(1,1)}} - 2\phi^{(2,2)}\mathscr{L}_1\mathscr{D}\overline{\phi^{(1,1)}} + \overline{\phi^{(1,1)}}\mathscr{L}_2\mathscr{D}\phi^{(2,2)}), \tag{4.10b}$$

$$\mathscr{N}_E^{01} = -\sqrt{2}\mathrm{i}(\mathscr{D}\phi^{(0,2)} + \mathscr{D}\overline{\phi^{(0,2)}})\varphi^{(1,1)} - \frac{4\sqrt{2}}{\alpha G}(\lambda-1)(\mathscr{D}\phi^{(0,2)} + \mathscr{D}\overline{\phi^{(0,2)}})\varphi^{(1,1)}, \tag{4.10c}$$

$$\mathscr{N}_E^{10} = \sqrt{2}\mathrm{i}\phi^{(1,1)}(\mathscr{D}\varphi^{(0,2)} + \mathscr{D}\overline{\varphi^{(0,2)}}) - \frac{4\sqrt{2}}{\alpha G}(\lambda-1)\mathscr{D}\phi^{(1,1)}(\varphi^{(0,2)} + \overline{\varphi^{(0,2)}}), \tag{4.10d}$$

$$\mathscr{N}_E^{12} = -\sqrt{2}\mathrm{i}(2\mathscr{D}\overline{\phi^{(1,1)}}\varphi^{(2,2)} + \overline{\phi^{(1,1)}}\mathscr{D}\varphi^{(2,2)}) - \frac{4\sqrt{2}}{\alpha G}(\lambda-1)\mathscr{D}\overline{\phi^{(1,1)}}\varphi^{(2,2)}, \tag{4.10e}$$

$$\mathscr{N}_E^{21} = \sqrt{2}\mathrm{i}(\mathscr{D}\phi^{(2,2)}\overline{\varphi^{(1,1)}} + 2\phi^{(2,2)}\mathscr{D}\overline{\varphi^{(1,1)}}) - \frac{4\sqrt{2}}{\alpha G}(\lambda-1)\mathscr{D}\phi^{(2,2)}\overline{\varphi^{(1,1)}}. \tag{4.10f}$$

The subscripts M and E refer to terms that originate from the momentum and energy equations. The superscripts 0, 1 and 2 represent the modification of the mean flow, fundamental mode and second harmonic, respectively. For example, in the energy equation, $\mathscr{N}_E^{01}$ is the interaction of the modification of the mean flow for velocity with the fundamental mode for temperature.

Equation (4.7) is an inhomogeneous differential equation that has a unique solution if and only if a solvability condition or the Fredholm alternative is satisfied. The solvability condition states that the inhomogeneous term has to be orthogonal to the solution of the adjoint homogeneous problem. The homogeneous adjoint problem associated with (4.7) is given as

$$\boldsymbol{Q}^{(1,3)^\dagger}\boldsymbol{X}^{(1,3)^\dagger} = 0, \tag{4.11}$$

where $\boldsymbol{X}^{(1,3)^\dagger} = (\phi^{(1,3)^\dagger}, \varphi^{(1,3)^\dagger})^{\mathrm{T}}$ and the adjoint operator $\boldsymbol{Q}^{(1,3)^\dagger}$ is defined through the relationship

$$\langle f, \mathscr{L}g\rangle = \langle \mathscr{L}^\dagger f, g\rangle. \tag{4.12}$$

Thus, $\boldsymbol{Q}^{(1,3)^\dagger}$ can be obtained by integration by parts. Then we obtain

$$\boldsymbol{Q}^{(1,3)^\dagger} = \begin{pmatrix} \dfrac{1}{G}\mathscr{L}_1^2 - \overline{\mathscr{M}^{(1,3)}}\mathscr{L}_1 + 2\mathrm{i}\alpha F_0''\mathscr{D} & -\sqrt{2}\mathrm{i}H_0' + \dfrac{4\sqrt{2}}{\alpha G}[\mathscr{D} + (\lambda-1)(H_0\mathscr{D} + H_0')] \\ -\dfrac{\alpha}{\sqrt{2}G}\mathscr{D} & \dfrac{1}{Pr\,G}\mathscr{L}_1 - \overline{\mathscr{M}^{(1,3)}} - \dfrac{4}{G}(\lambda-1)F_0' \end{pmatrix}, \tag{4.13}$$

with the adjoint boundary conditions

$$\phi^{(1,3)^\dagger}(0) = \mathscr{D}\phi^{(1,3)^\dagger}(0) = \mathscr{D}\phi^{(1,3)^\dagger}(\infty) = \varphi^{(1,3)^\dagger}(0) = \varphi^{(1,3)^\dagger}(\infty) = 0. \tag{4.14}$$

The amplitude of the adjoint solution is normalized by

$$\langle \phi^{(1,3)^\dagger}, \phi^{(1,3)^\dagger}\rangle + \langle \varphi^{(1,3)^\dagger}, \varphi^{(1,3)^\dagger}\rangle = 1. \tag{4.15}$$

The adjoint solutions $\phi^{(1,3)^\dagger}$ and $\varphi^{(1,3)^\dagger}$ for $Pr = 6.7$ with different λ are displayed in figure 10 in Appendix B. The Fredholm alternative for the present case means that the right-hand side of (4.7) has to be orthogonal to the solution of the adjoint problem (4.11).

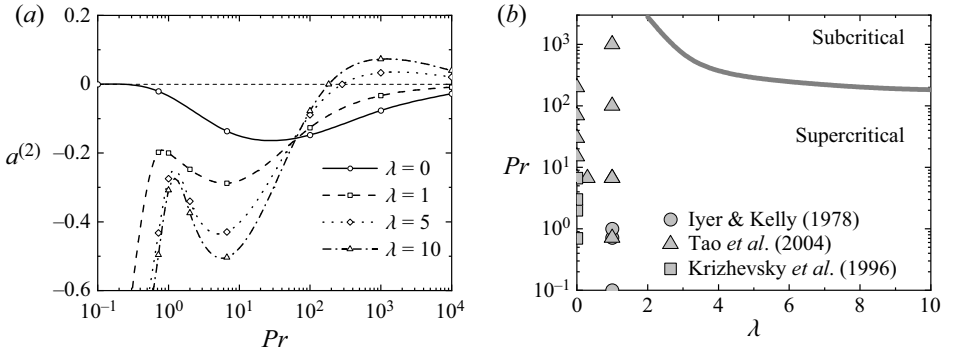

Figure 7. (*a*) Variation of the Landau coefficient $a^{(2)}$ with Pr for different λ. The lines are obtained by spline interpolation. (*b*) Phase diagram in the (Pr, λ) plane. The grey thick solid line indicates the boundary $a^{(2)} = 0$ separating the supercritical region (below) and subcritical region (above).

The Landau coefficient is then obtained:

$$a^{(2)} + \mathrm{i}b^{(2)} = -\frac{\langle \boldsymbol{X}^{(1,3)\dagger}, \boldsymbol{F}^{(1,3)} \rangle}{\langle \boldsymbol{X}^{(1,3)\dagger}, \boldsymbol{S}\boldsymbol{X}^{(1,1)} \rangle} = \sigma_M^{01} + \sigma_M^{12} + \sigma_E^{01} + \sigma_E^{10} + \sigma_E^{12} + \sigma_E^{21}, \tag{4.16}$$

with

$$\sigma_M^{01} = -\frac{\langle \phi^{(1,3)\dagger}, \mathscr{N}_M^{01} \rangle}{\langle \boldsymbol{X}^{(1,3)\dagger}, \boldsymbol{S}\boldsymbol{X}^{(1,1)} \rangle}, \quad \sigma_M^{12} = -\frac{\langle \phi^{(1,3)\dagger}, \mathscr{N}_M^{12} \rangle}{\langle \boldsymbol{X}^{(1,3)\dagger}, \boldsymbol{S}\boldsymbol{X}^{(1,1)} \rangle}, \tag{4.17a}$$

$$\sigma_E^{01} = -\frac{\langle \varphi^{(1,3)\dagger}, \mathscr{N}_E^{01} \rangle}{\langle \boldsymbol{X}^{(1,3)\dagger}, \boldsymbol{S}\boldsymbol{X}^{(1,1)} \rangle}, \quad \sigma_E^{10} = -\frac{\langle \varphi^{(1,3)\dagger}, \mathscr{N}_E^{10} \rangle}{\langle \boldsymbol{X}^{(1,3)\dagger}, \boldsymbol{S}\boldsymbol{X}^{(1,1)} \rangle}, \tag{4.17b}$$

$$\sigma_E^{12} = -\frac{\langle \varphi^{(1,3)\dagger}, \mathscr{N}_E^{12} \rangle}{\langle \boldsymbol{X}^{(1,3)\dagger}, \boldsymbol{S}\boldsymbol{X}^{(1,1)} \rangle}, \quad \sigma_E^{21} = -\frac{\langle \varphi^{(1,3)\dagger}, \mathscr{N}_E^{21} \rangle}{\langle \boldsymbol{X}^{(1,3)\dagger}, \boldsymbol{S}\boldsymbol{X}^{(1,1)} \rangle}, \tag{4.17c}$$

where σ_M^{01} is the feedback of the mean flow distortion on the fundamental mode, σ_E^{12} is the feedback of the second harmonic on the fundamental mode, etc. The supercritical and subcritical types of instability (bifurcation) are identified by the sign of $a^{(2)}$. For $a^{(0)} > 0$ and $a^{(2)} < 0$, a finite-amplitude equilibrium solution can be achieved after the infinitesimal state has become unstable, which is known as supercritical bifurcation. For $a^{(0)} < 0$ and $a^{(2)} > 0$, a finite-amplitude equilibrium solution can be achieved before the base state has become linearly unstable, which is known as subcritical bifurcation.

Utilizing the numerical values in table 2, $a^{(2)}$ and $b^{(2)}$ are computed over a range of critical parameters. Several tests are performed for different computational domains η_{max} and Chebyshev points N to ensure numerical convergence, and the results are shown in table 4 in Appendix C. The result of the Landau coefficient $a^{(2)}$ from (4.16) for different Pr and λ at the least unstable parameter is shown in figure 7(*a*). For the isothermal ($\lambda = 0$) and uniform-heat-flux ($\lambda = 1$) walls, we found that $a^{(2)} < 0$ for all the cases ($10^{-1} \leqslant Pr \leqslant 10^4$) considered here, which means the flow is supercritical instability. However, with an increase in the temperature gradient ratio, $a^{(2)} > 0$ is obtained for a large value of Pr and this corresponds to the subcritical solution. The results are therefore limited to $Pr \leqslant 10^4$.

The boundary $a^{(2)} = 0$ is shown in figure 7(*b*), which separates the (Pr, λ) plane into a supercritical region (below) and subcritical region (above). It can be seen that, for

Pr	λ	G_c	α_c	$c_c^{(0)}$	$a^{(2)}$	$b^{(2)}$
0.10	0	24.85	0.0655	2.6916	−0.0001	0.0007
0.72	0	24.69	0.2800	0.4795	−0.0207	0.0130
6.70	0	28.79	0.6850	0.1407	−0.1366	0.0118
100.00	0	41.79	1.4190	0.0387	−0.1474	0.1059
1000.00	0	70.48	2.4300	0.0126	−0.0766	0.1987
0.10	1	38.60	0.3310	0.2724	−1.7054	2.5603
0.72	1	158.16	0.2678	0.1649	−0.1979	0.0695
6.70	1	99.55	0.6684	0.0762	−0.2877	0.0549
100.00	1	107.50	1.4500	0.0236	−0.3645	−0.1399
1000.00	1	171.14	2.4180	0.0079	−0.0333	−0.1749
0.10	5	318.00	0.4130	0.0888	−1.4844	3.0643
0.72	5	585.26	0.3560	0.0706	−0.4322	−0.0614
6.70	5	321.96	0.8050	0.0410	−0.4296	−0.0297
100.00	5	281.31	1.6900	0.0139	−0.0887	−0.2399
1000.00	5	421.19	2.6700	0.0048	0.0336	−0.5933
0.10	10	567.89	0.4790	0.0611	−1.3107	2.8411
0.72	10	1001.96	0.4150	0.0496	−0.4962	−0.1402
6.70	10	557.57	0.9350	0.0302	−0.5037	−0.1382
100.00	10	461.01	1.8840	0.0106	−0.0775	−0.3218
1000.00	10	670.52	2.8650	0.0037	0.0730	−0.7891

Table 2. Critical Grashof number G_c, critical wavenumber α_c, critical phase velocity $c_c^{(0)}$ and Landau coefficient for different Prandtl number Pr and temperature gradient ratio λ.

$0 \leqslant \lambda < 2$, only a supercritical bifurcation exists when $Pr \leqslant 2800$. Moreover, with an increase of temperature gradient ratio, the corresponding value of Pr at the boundary gradually decreases. It is illustrated in figure 7(*b*) that subcritical bifurcations are observed only for large temperature gradient ratios and Prandtl numbers. Close examination for basic flow $F_0'(\eta)$ and $H_0(\eta)$ reveals that for higher temperature gradient ratio and Prandtl number, the position of the maximum amplitude of velocity moves towards the wall and the temperature gradients near the wall increase due to a thinner boundary layer. And the absolute values of the maximum and the minimum streamwise velocities also decrease with an increase of Pr and λ. These characteristics of basic flow may be related to the fact of the existence of subcritical bifurcation at high Pr and λ. It is worth mentioning that the parameter values from Iyer & Kelly (1978) all lie within the region where the bifurcation is supercritical, which is consistent with their results. Besides, the parameter values for the discussion on the convective and absolute instabilities from Krizhevsky *et al.* (1996) and Tao *et al.* (2004*b*) are also shown in figure 7(*b*). The bifurcation types corresponding to these parameters are still supercritical. In fact, the above results suggest that most common fluids, such as air ($Pr = 0.72$), water ($Pr = 6.7$) and argon ($Pr = 23$), are below the boundary and belong to supercritical bifurcation. For fluids such as glycerine ($Pr \approx 2000$), the buoyancy layer can experience a subcritical bifurcation under a larger temperature gradient ratio.

4.4. *Threshold amplitude*

In this subsection, we discuss the nature of bifurcation for the appearance of finite-amplitude nonlinear equilibrium solutions. We rewrite the Landau equation

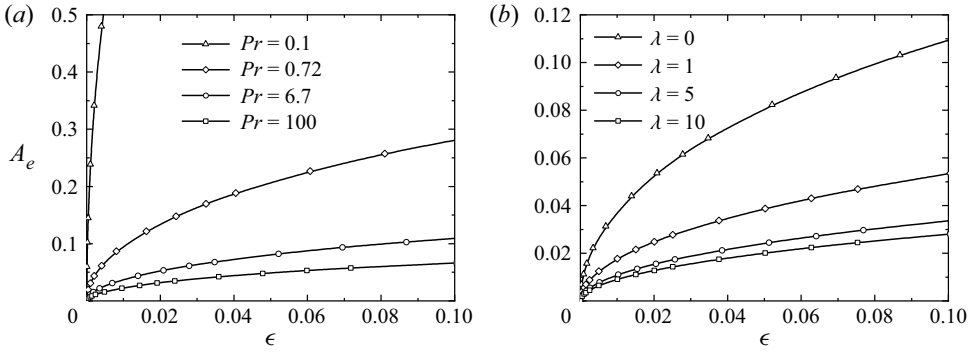

Figure 8. Variation of equilibrium amplitude as a function of $\epsilon = (G - G_c)/G_c$ for (*a*) $\lambda = 0$ with different Pr and (*b*) $Pr = 6.7$ with different λ. The bifurcation is supercritical in each case.

(2.13*a*,*b*) as

$$\frac{\mathrm{d}A}{\mathrm{d}\tau} = Aa^{(0)} + A^3 a^{(2)} + A^5 a^{(4)} + \cdots . \tag{4.18}$$

This series is also known as the Stuart–Landau series (Stuart 1960; Watson 1960), in which $a^{(0)}$ is the growth rate from linear theory and the Landau coefficients $a^{(2)}, a^{(4)}, \ldots$ are nonlinear corrections to the linear growth rate as mentioned above. Only the leading-order term of the Landau coefficient is of concern here and the stationary equilibrium amplitude solution A_e for (4.18) has two possible solutions. If $a^{(0)}$ and $a^{(2)}$ are of the same sign, only the zero-amplitude state exists as an equilibrium solution. If $a^{(0)}$ and $a^{(2)}$ are of opposite sign, as time increases, we have a steady state:

$$A_e = \sqrt{-\frac{a^{(0)}}{a^{(2)}}}. \tag{4.19}$$

Figure 8 plots the equilibrium amplitude A_e in the neighbourhood of the critical instability $\epsilon = (G - G_c)/G_c \ll 1$ for different values of λ and Pr when the instabilities are supercritical. The equilibrium amplitude increases smoothly with an increase of ϵ, and we have $A_e \sim \epsilon^{-1/2}$ according to the Taylor expansion. For given λ and Pr, the threshold amplitude will reach a stable nonlinear state, which limits the basin of attraction of the laminar flow. When $\lambda = 0$, the equilibrium amplitude decreases with an increase of Pr (see figure 8*a*), i.e. the flow becomes more sensitive to small perturbations. Figure 8(*b*) illustrates that A_e decreases significantly as the temperature gradient ratio increases. Apparently, the magnitude of A_e for the flow near an isothermal wall is twice that for a uniform-heat-flux wall.

Figure 9 shows a series of bifurcation diagrams for six values of Pr at $\lambda = 5$. It can be seen that, with increasing Pr, the equilibrium amplitude increases gradually when the flow works in the linearly unstable regime $\epsilon > 0$. The instability here is of supercritical type, which is indicated by solid lines in figure 9. However, when the value of Pr continues to increase, the bifurcation type becomes subcritical immediately (dashed lines) and the value of A_e decreases. It is noteworthy that the buoyancy flow is nonlinearly stable for $A < A_e$ and unstable for $A > A_e$, and the finite-amplitude unstable branch in figure 9 provides a threshold for nonlinear stability. It is obtained that the critical Prandtl number at which this switchover between the subcritical and supercritical bifurcations occurs is $Pr \approx 285$.

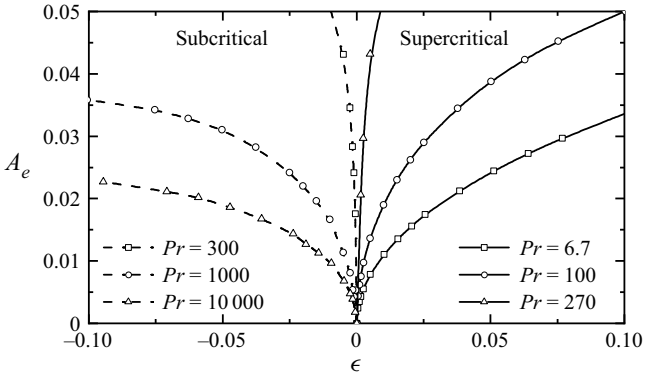

Figure 9. Variation of equilibrium amplitude as a function of $\epsilon = (G - G_c)/G_c$ for $\lambda = 5$ with different Pr. The bifurcation type changes from supercritical (solid lines) to subcritical (dashed lines).

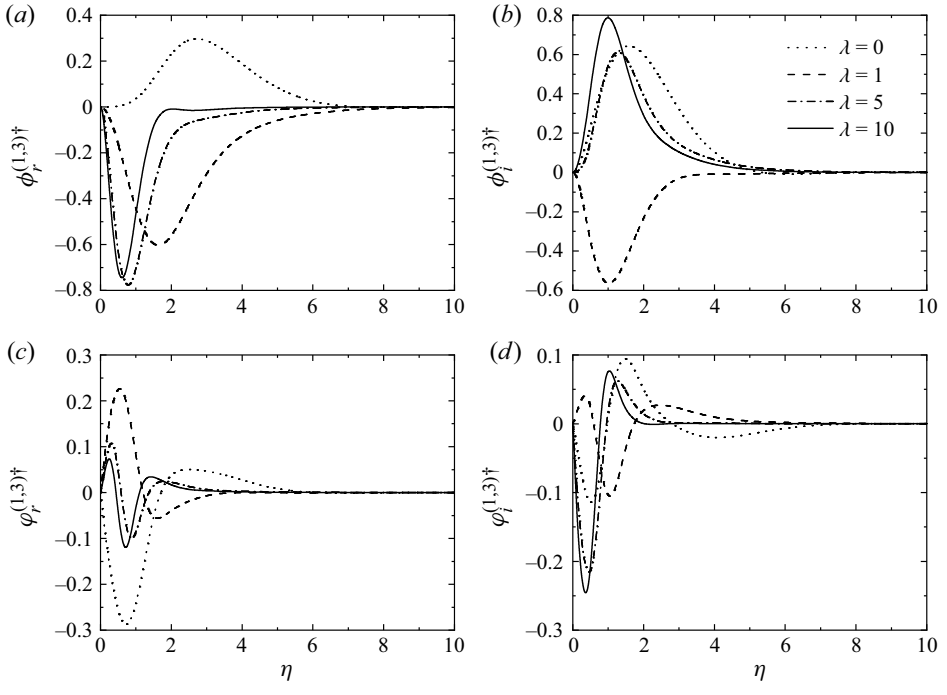

Figure 10. Adjoint eigenfunctions for $Pr = 6.7$. (*a*) Real and (*b*) imaginary parts of $\phi^{(1,3)\dagger}$. (*c*) Real and (*d*) imaginary parts of $\varphi^{(1,3)\dagger}$.

In order to analyse the nonlinear effects that control the type of bifurcation, the contributions of the different terms $\sigma_M^{01}, \sigma_M^{12}, \ldots$ in (4.16) that affect the value of $a^{(2)}$ are given in table 3 for the parameters analysed in figure 9. There are several points worth noting. First, the fundamental modes $\phi^{(1,1)}$ in the momentum equation play a minor role in these effects since the corresponding contributions σ_M^{01} and σ_M^{12} are of small magnitude in comparison with the contributions associated with that in the energy equation. A second important point is that the values of σ_E^{10} and σ_E^{12} are always negative, which means the interaction between the fundamental mode for velocity and temperature

Pr	$a^{(2)}$	σ_M^{01}	σ_M^{12}	σ_E^{01}	σ_E^{10}	σ_E^{12}	σ_E^{21}
6.7	−0.4296	0.0322	−0.0113	0.1182	−0.3910	−0.1100	−0.0677
100.0	−0.0887	0.0081	−0.0149	0.1139	−0.1640	−0.0784	0.0467
270.0	−0.0041	−0.0056	−0.0113	0.0855	−0.0770	−0.0534	0.0577
300.0	0.0035	−0.0062	−0.0109	0.0825	−0.0700	−0.0497	0.0578
1000.0	0.0336	−0.0080	−0.0069	0.0523	−0.0265	−0.0261	0.0487
10 000.0	0.0203	−0.0034	−0.0024	0.0181	−0.0061	−0.0064	0.0205

Table 3. Landau coefficient and real part of the contribution of the nonlinear terms for different Prandtl number Pr at temperature gradient ratio $\lambda = 5$.

is beneficial to supercritical bifurcation. A last important point revealed in table 3 is that the buoyancy-driven effects are crucial since for different Pr, the values of $\sigma_E^{01} + \sigma_E^{21}$ are greater than zero. The flow energy from distortion of the mean flow $\phi^{(0,2)}$ to the fundamental $\varphi^{(1,1)}$ is described by σ_E^{01}, while σ_E^{21} represents the flow energy from the fundamental $\varphi^{(1,1)}$ to the second harmonic $\phi^{(2,2)}$. This suggests that the interaction of the modification of the mean flow and second harmonic for velocity with the fundamental mode for temperature plays an important role in the subcritical bifurcation. Considering that the buoyancy-driven instability becomes increasingly important as the Prandtl number is increased (Gill & Davey 1969), the coupling between the energy equation and the Orr–Sommerfeld equation may provide some clues for revealing the mechanism of changing bifurcation.

5. Conclusion

In this work, we have studied the finite-amplitude instability of the natural convection flow on a vertically heated plate, where the ambient fluid and the wall have independent temperature gradients. As mentioned in the introduction, the linear stability was investigated by Tao *et al.* (2004*b*), and the finite-amplitude solution (Iyer & Kelly 1978) arising from the critical instability was studied only for a uniform-heat-flux surface ($\lambda = 1$). Only supercritical bifurcation was found in their analysis. In order to extend their results, a weakly nonlinear theory is developed to describe the nonlinear instability of the buoyancy-driven boundary layer. The amplitude expansion method of Reynolds & Potter (1967) is adapted to the present nonlinear problem. At different orders, the nonlinear stability problem is reduced to a sequence of linear inhomogeneous differential equations. Then, the basic flow, the fundamental mode, the related modification of the base flow, the second harmonics and Landau coefficients are obtained.

The flow is governed by three parameters: modified Grashof number G, Prandtl number Pr and temperature gradient ratio λ. The present parametric study is mainly focused on the critical mode of the linear problem, except in the discussion on equilibrium amplitude. The main conclusions of the analysis are as follows. For the distortion of mean flow, the maximum value of the correction amount of velocity and temperature increases with an increase of λ for fixed $Pr = 6.7$. With an increase of Pr, the maximum value of the distortion of mean flow increases constantly for the isothermal surface. For the second harmonic generated by the fundamental mode interacting with itself, when $Pr = 6.7$, the position of the second and third peaks of velocity almost coincides with the extreme position of the linear mode corresponding to the buoyancy-driven instability mode. And the modulus of the harmonic increases with increasing λ. The Landau coefficients are

determined from the solvability condition (the Fredholm alternative) at $O(A^3)$. We have identified the boundary for Landau coefficient $a^{(2)} = 0$. For Prandtl number above the critical value, the bifurcation is subcritical. Otherwise, it is a supercritical bifurcation. It is shown that, for $0 \leqslant \lambda < 2$, only supercritical bifurcation exists when $Pr \leqslant 2800$. The current result is consistent with that of Iyer & Kelly (1978). In addition, the threshold amplitude of the bifurcation is determined as well. The threshold amplitude decreases with increasing Pr for the isothermal wall. For $Pr = 6.7$, the threshold amplitude also decreases with increasing λ. By analysing the contribution of the nonlinear terms in the Landau coefficient for the bifurcation type changing from supercritical to subcritical, it is revealed that the interaction of the modification of the mean flow and second harmonic for velocity with the fundamental mode for temperature plays an important role in subcritical bifurcation.

Although only two-dimensional disturbances are considered in this paper, the present configuration can be extended to analyse the finite-amplitude instability in the three-dimensional buoyancy layer. We have only calculated the first Landau coefficient at cubic order in A. For subcritical bifurcations and significant deviation from the critical parameter, the higher-order Landau coefficients are needed to identify the stable finite-amplitude solution. Despite this, we anticipate that the results provided in this paper may serve as a guide for the sequence of bifurcation leading to turbulence for such a buoyancy-driven flow system. We emphasize that the experimental data in the literature are very scarce. This is also very convenient and helpful in the experimental study of near-onset dynamics, in particular, for high-Prandtl-number fluids for which the bifurcation should be subcritical. This will be the subject of future exploration.

Funding. This work was supported by the National Natural Science Foundation of China (no. 12072177).

Declaration of interests. The authors have no conflicts to disclose.

Author ORCIDs.
Yue Xiao https://orcid.org/0000-0002-2472-9686.

Appendix A. The equations for $\boldsymbol{\phi}^{(k,n)}(\eta)$ and $\boldsymbol{\varphi}^{(k,n)}(\eta)$

The ordinary differential equations for $\phi^{(k,n)}(\eta)$ and $\varphi^{(k,n)}(\eta)$ are as follows:

$$\underbrace{\frac{\mathrm{d}A}{\mathrm{d}t}\frac{\partial\zeta}{\partial A}}_{T_1} + \underbrace{\left[\omega + \frac{\mathrm{d}\omega}{\mathrm{d}A}\left(t\frac{\mathrm{d}A}{\mathrm{d}t}\right)\right]\frac{\partial\zeta}{\partial\theta}}_{T_2} + \underbrace{\frac{\partial\psi}{\partial\eta}\frac{\partial\zeta}{\partial\theta}}_{N_1} - \underbrace{\frac{\partial\psi}{\partial\theta}\frac{\partial\zeta}{\partial\eta}}_{N_2} = \underbrace{\frac{1}{G}\nabla_\alpha^2\zeta}_{D_1} + \underbrace{\frac{\alpha}{\sqrt{2}G}\frac{\partial T}{\partial\eta}}_{R_1}, \tag{A1a}$$

$$\underbrace{\frac{\mathrm{d}A}{\mathrm{d}t}\frac{\partial T}{\partial A}}_{T_3} + \underbrace{\left[\omega + \frac{\mathrm{d}\omega}{\mathrm{d}A}\left(t\frac{\mathrm{d}A}{\mathrm{d}t}\right)\right]\frac{\partial T}{\partial\theta}}_{T_4} + \underbrace{\frac{\partial\psi}{\partial\eta}\frac{\partial T}{\partial\theta}}_{N_3} - \underbrace{\frac{\partial\psi}{\partial\theta}\frac{\partial T}{\partial\eta}}_{N_4}$$

$$= \underbrace{\frac{1}{Pr\,G}\nabla_\alpha^2 T}_{D_2} - \underbrace{\frac{4\sqrt{2}\varepsilon[1+(\lambda-1)T]}{\alpha f}\frac{\partial\psi}{\partial\eta}}_{R_2} + O(\varepsilon^2), \tag{A1b}$$

where the additional terms at $O(\varepsilon^2)$ are ignored. We separate each term of (A1) with

$$T_1 = 2\alpha^2 \frac{f_\theta}{f} \mathrm{i}k \sum_{q=k}^{n} q a^{(n-q)} \phi^{(k,q)} + \sum_{q=k}^{n} q a^{(n-q)} \mathscr{L}_k \phi^{(k,q)}, \tag{A2}$$

$$T_2 = \frac{f_\theta}{f} \sum_{q=k}^{n} b^{(n-q)} (\mathscr{L}_k - 2k^2\alpha^2) \phi^{(k,q)} + \mathrm{i}k \sum_{q=k}^{n} b^{(n-q)} \mathscr{L}_k \phi^{(k,q)}, \tag{A3}$$

$$\begin{aligned}
N_1 = \sqrt{2} \Bigg\{ & \sum_{j=0}^{k} \sum_{q=j}^{n-k+j} \mathscr{D}\phi^{(k-j,n-q)} \mathrm{i}j \mathscr{L}_j \phi^{(j,q)} \\
& + \frac{1}{1+\delta_{k0}} \Bigg[\sum_{j=0}^{\infty} \sum_{q=k+j}^{n-j} \mathscr{D}\overline{\phi^{(j,n-q)}} \mathrm{i}(k+j) \mathscr{L}_{k+j} \phi^{(k+j,q)} \\
& - \sum_{j=0}^{\infty} \sum_{q=j}^{n-k-j} \mathscr{D}\phi^{(k+j,n-q)} \mathrm{i}j \mathscr{L}_j \overline{\phi^{(j,q)}} \Bigg] \Bigg\} \\
& + \sqrt{2} \frac{f_\theta}{f} \Bigg\{ \sum_{j=0}^{k} \sum_{q=j}^{n-k+j} \mathscr{D}\phi^{(k-j,n-q)} (\mathscr{L}_j - 2j^2\alpha^2) \phi^{(j,q)} \\
& + \frac{1}{1+\delta_{k0}} \Bigg[\sum_{j=0}^{\infty} \sum_{q=k+j}^{n-j} \mathscr{D}\overline{\phi^{(j,n-q)}} (\mathscr{L}_{k+j} - 2(k+j)^2\alpha^2) \phi^{(k+j,q)} \\
& + \sum_{j=0}^{\infty} \sum_{q=j}^{n-k-j} \mathscr{D}\phi^{(k+j,n-q)} (\mathscr{L}_j - 2j^2\alpha^2) \overline{\phi^{(j,q)}} \Bigg] \Bigg\},
\end{aligned} \tag{A4}$$

$$\begin{aligned}
N_2 = \sqrt{2} \Bigg\{ & \sum_{j=0}^{k} \sum_{q=j}^{n-k+j} \mathrm{i}(k-j) \phi^{(k-j,n-q)} \mathscr{L}_j \mathscr{D}\phi^{(j,q)} \\
& + \frac{1}{1+\delta_{k0}} \Bigg[\sum_{j=0}^{\infty} \sum_{q=j}^{n-k-j} \mathrm{i}(k+j) \phi^{(k+j,n-q)} \mathscr{L}_j \mathscr{D}\overline{\phi^{(j,q)}} \\
& - \sum_{j=0}^{\infty} \sum_{q=k+j}^{n-j} \mathrm{i}j \overline{\phi^{(j,n-q)}} \mathscr{L}_{k+j} \mathscr{D}\phi^{(k+j,q)} \Bigg] \Bigg\} \\
& + \sqrt{2} \frac{f_\theta}{f} \Bigg[\sum_{j=0}^{k} \sum_{q=j}^{n-k+j} \phi^{(k-j,n-q)} \mathscr{L}_j \mathscr{D}\phi^{(j,q)}
\end{aligned}$$

$$+\frac{1}{1+\delta_{k0}}\left(\sum_{j=0}^{\infty}\sum_{q=k+j}^{n-j}\overline{\phi^{(j,n-q)}}\mathscr{L}_{k+j}\mathscr{D}\phi^{(k+j,q)}+\sum_{j=0}^{\infty}\sum_{q=j}^{n-k-j}\phi^{(k+j,n-q)}\mathscr{L}_j\mathscr{D}\overline{\phi^{(j,q)}}\right)\Bigg]$$
$$+2\sqrt{2}\alpha^2\frac{f_\theta}{f}\left\{-\sum_{j=0}^{k}\sum_{q=j}^{n-k+j}(k-j)j\phi^{(k-j,n-q)}\mathscr{D}\phi^{(j,q)}\right.$$
$$+\frac{1}{1+\delta_{k0}}\left[\sum_{j=0}^{\infty}\sum_{q=k+j}^{n-j}j(k+j)\overline{\phi^{(j,n-q)}}\mathscr{D}\phi^{(k+j,q)}\right.$$
$$\left.\left.+\sum_{j=0}^{\infty}\sum_{q=j}^{n-k-j}(k+j)j\phi^{(k+j,n-q)}\mathscr{D}\overline{\phi^{(j,q)}}\right]\right\}, \tag{A5}$$

$$D_1=\frac{1}{G}\left(4\alpha^2\frac{f_\theta}{f}\mathrm{i}k\mathscr{L}_k\phi^{(k,n)}+\mathscr{L}_k^2\phi^{(k,n)}\right),\quad R_1=\frac{\alpha}{\sqrt{2}G}\mathscr{D}\varphi^{(k,n)}, \tag{A6a,b}$$

$$T_3=\sum_{q=k}^{n}qa^{(n-q)}\varphi^{(k,q)},\quad T_4=\mathrm{i}k\sum_{q=k}^{n}b^{(n-q)}\varphi^{(k,q)},\quad D_2=\frac{1}{Pr\,G}\mathscr{L}_k\varphi^{(k,n)}, \tag{A7a–c}$$

$$N_3=\sqrt{2}\left\{\sum_{j=0}^{k}\sum_{q=j}^{n-k+j}\mathscr{D}\phi^{(k-j,n-q)}\mathrm{i}j\varphi^{(j,q)}\right.$$
$$\left.+\frac{1}{1+\delta_{k0}}\left[\sum_{j=0}^{\infty}\sum_{q=k+j}^{n-j}\mathscr{D}\overline{\phi^{(j,n-q)}}\mathrm{i}(k+j)\varphi^{(k+j,q)}-\sum_{j=0}^{\infty}\sum_{q=j}^{n-k-j}\mathscr{D}\phi^{(k+j,n-q)}\mathrm{i}j\overline{\varphi^{(j,q)}}\right]\right\}, \tag{A8}$$

$$N_4=\sqrt{2}\left\{\sum_{j=0}^{k}\sum_{q=j}^{n-k+j}\mathrm{i}(k-j)\phi^{(k-j,n-q)}\mathscr{D}\varphi^{(j,q)}\right.$$
$$\left.+\frac{1}{1+\delta_{k0}}\left[\sum_{j=0}^{\infty}\sum_{q=j}^{n-k-j}\mathrm{i}(k+j)\phi^{(k+j,n-q)}\mathscr{D}\overline{\varphi^{(j,q)}}-\sum_{j=0}^{\infty}\sum_{q=k+j}^{n-j}\mathrm{i}j\overline{\phi^{(j,n-q)}}\mathscr{D}\varphi^{(k+j,q)}\right]\right\}$$
$$+\sqrt{2}\frac{f_\theta}{f}\left[\sum_{j=0}^{k}\sum_{q=j}^{n-k+j}\phi^{(k-j,n-q)}\mathscr{D}\varphi^{(j,q)}\right.$$

Paremeters	$a^{(0)}$	$b^{(0)}$	$a^{(2)}$	$b^{(2)}$	η_{max}	N
	-6.47×10^{-4}	-0.1336	-0.0204	0.0127	10	50
	-5.18×10^{-7}	-0.1343	-0.0207	0.0130	20	50
$Pr=0.72$	-5.11×10^{-7}	-0.1343	-0.0207	0.0130	20	100
$\lambda=0$	-5.67×10^{-8}	-0.1343	-0.0207	0.0130	40	100
	-1.09×10^{-7}	-0.1343	-0.0207	0.0130	**40**	**200**
	-3.62×10^{-8}	-0.1343	-0.0207	0.0130	60	400
	-1.34×10^{-4}	-0.0509	-0.2841	0.0527	5	50
	-1.80×10^{-7}	-0.0510	-0.2879	0.0549	10	50
$Pr=6.7$	-1.78×10^{-7}	-0.0510	-0.2878	0.0549	10	100
$\lambda=1$	-8.03×10^{-8}	-0.0510	-0.2878	0.0549	20	100
	-6.36×10^{-8}	-0.0510	-0.2877	0.0549	**20**	**200**
	$+5.77\times10^{-7}$	-0.0510	-0.2877	0.0549	40	400

Table 4. Numerical values of $a^{(0)}$, $b^{(0)}$, $a^{(2)}$ and $b^{(2)}$ for critical instabilities at different computational domains η_{max} and Chebyshev points N for two sets of typical parameters. The number of Chebyshev points $N=200$ is used in calculations, which is marked in bold.

$$+\frac{1}{1+\delta_{k0}}\left(\sum_{j=0}^{\infty}\sum_{q=k+j}^{n-j}\overline{\phi^{(j,n-q)}}\mathscr{D}\varphi^{(k+j,q)}+\sum_{j=0}^{\infty}\sum_{q=j}^{n-k-j}\phi^{(k+j,n-q)}\mathscr{D}\overline{\varphi^{(j,q)}}\right)\Bigg], \tag{A9}$$

$$R_2=\frac{4\sqrt{2}\varepsilon}{\alpha f}\left\{\mathscr{D}\phi^{(k,n)}+(\lambda-1)\left[\sum_{j=0}^{k}\sum_{q=j}^{n-k+j}\varphi^{(k-j,n-q)}D\phi^{(j,q)}\right.\right.$$
$$\left.\left.+\frac{1}{1+\delta_{k0}}\left(\sum_{j=0}^{\infty}\sum_{q=k+j}^{n-j}\overline{\varphi^{(j,n-q)}}\mathscr{D}\phi^{(k+j,q)}+\sum_{j=0}^{\infty}\sum_{q=j}^{n-k-j}\varphi^{(k+j,n-q)}\mathscr{D}\overline{\phi^{(j,q)}}\right)\right]\right\}, \tag{A10}$$

where $\mathscr{L}_k=\mathscr{D}^2-k^2\alpha^2$, $\mathscr{D}=\mathrm{d}/\mathrm{d}\eta$ and $\delta_{kj}=0$ if $k\neq j$, $\delta_{kj}=1$ if $k=j$. The overbar denotes complex conjugation. The factor $1/(1+\delta_{k0})$ in the above equations arises from the product of two Fourier series in which the zeroth-order terms are multiplied by a factor of 2. The corresponding boundary conditions for $k,n\geqslant1$ are

$$\phi^{(k,n)}(0)=\mathscr{D}\phi^{(k,n)}(0)=\mathscr{D}\phi^{(k,n)}(\infty)=\varphi^{(k,n)}(0)=\varphi^{(k,n)}(\infty)=0. \tag{A11}$$

Appendix B. Adjoint eigenfunctions for $\boldsymbol{\phi}^{(1,3)\dagger}$ and $\boldsymbol{\varphi}^{(1,3)\dagger}$

The eigenfunctions of the adjoint linear operator $\boldsymbol{Q}^{(1,3)\dagger}$ in (4.13) for $Pr=6.7$ with different temperature gradient are shown in figure 10.

Appendix C. Numerical convergence tests

Table 4 shows the results of numerical convergence tests for different computational domains η_{max} and Chebyshev points N.

References

Candelier, J., LeDizès, S. & Millet, C. 2012 Inviscid instability of a stably stratified compressible boundary layer on an inclined surface. *J. Fluid Mech.* **694**, 524–539.

Chen, J., Bai, Y. & LeDizès, S. 2016 Instability of a boundary layer flow on a vertical wall in a stably stratified fluid. *J. Fluid Mech.* **795**, 262–277.

Chen, Y.C. & Chung, J.N. 2002 A direct numerical simulation of K and H-type flow transition in heated vertical channel. *Phys. Fluids* **14**, 3327–3346.

Chen, Y.C. & Chung, J.N. 2003 A direct numerical simulation of transition phenomena in a mixed convection channel flow. *Comput. Fluids* **32**, 795–822.

Desrayaud, G. 1990 Stability of flow near a heat-flux plate and comparison with numerical simulations in a square cavity. *Tech. Rep.* 1990/LT/01. CNAM.

Gebhart, B., Jaluria, Y., Mahajan, R.L. & Samumakia, B. 1993 *Buoyancy Induced Flows and Transport*. Hemisphere.

Gill, A.E. 1966 The boundary-layer regime for convection in a rectangular cavity. *J. Fluid Mech.* **26**, 515–536.

Gill, A.E. & Davey, A. 1969 Instabilities of a buoyancy-driven system. *J. Fluid Mech.* **35**, 775–798.

Iyer, P.A. 1973 Instabilities in buoyancy-driven boundary-layer flows in a stably stratified medium. *Boundary-Layer Meteorol.* **5**, 53–66.

Iyer, P.A. & Kelly, R.E. 1978 Supercritical solutions for the buoyancy boundary layer. *Trans. ASME J. Heat Transfer* **100**, 648–652.

Jaluria, Y. & Gebhart, B. 1974 Stability and transition of buoyancy induced flows in a stratified medium. *J. Fluid Mech.* **66**, 593–612.

Jaluria, Y. & Himasekhar, K. 1983 Buoyancy induced two dimensional vertical flows in a thermally stratified environment. *Comput. Fluids* **11**, 39–49.

Jeschke, P. & Beer, H. 2001 Longitudinal vortices in a laminar natural convection boundary layer flow on an inclined flat plate and their influence on heat transfer. *J. Fluid Mech.* **432**, 313–339.

Khandelwal, M.K. & Bera, P. 2015 Weakly nonlinear stability analysis of non-isothermal poiseuille flow in a vertical channel. *Phys. Fluids* **27**, 064103.

Krizhevsky, L., Cohen, J. & Tanny, J. 1996 Convective and absolute instabilities of a buoyancy-induced flow in a thermally stratified medium. *Phys. Fluids* **8**, 971–977.

Kulkarni, A.K., Jacobs, H.R. & Hwang, J.J. 1987 Similarity solution for natural convection flow over an isothermal vertical wall immersed in thermally stratified medium. *Int J. Heat Mass Transfer* **30**, 691–698.

McBain, G.D., Armfield, S.W. & Desrayaud, G. 2007 Instability of the buoyancy layer on an evenly heated vertical wall. *J. Fluid Mech.* **587**, 453–469.

Mizushima, J. & Gotoh, K. 1983 Nonlinear evolution of the disturbance in a natural convection induced in a vertical fluid layer. *J. Phys. Soc. Japan* **52**, 1206–1214.

Parente, E., Robinet, J.C., DePalma, P. & Cherubini, S. 2020 Modal and nonmodal stability of a stably stratified boundary layer flow. *Phys. Rev. Fluids* **5**, 113901.

Prandtl, L. 1952 *Essentials of Fluid Dynamics*. Blackie.

Prud'homme, M. & LeQuéré, P. 2007 Stability of stratified natural convection in a tall vertical annular cavity. *Phys. Fluids* **19**, 094106.

Reynolds, W.C. & Potter, M.C. 1967 Finite-amplitude instability of parallel shear flows. *J. Fluid Mech.* **27**, 465–492.

Schmid, P.J. & Henningson, D.S. 2001 *Stability and Transition in Shear Flows*. Springer.

Stuart, J.T. 1958 On the non-linear mechanics of hydrodynamic stability. *J. Fluid Mech.* **4**, 1–21.

Stuart, J.T. 1960 On the non-linear mechanics of wave disturbances in stable and unstable parallel flows Part 1. The basic behaviour in plane Poiseuille flow. *J. Fluid Mech.* **9**, 353–370.

Stull, R.B. 1989 *An Introduction to Boundary Layer Meteorology*. Academic.

Tao, J. & Busse, F.H. 2009 Oblique roll instability in inclined buoyancy layers. *Eur. J. Mech. (*B*/Fluids)* **28**, 532–540.

Tao, J., LeQuéré, P. & Xin, S. 2004*a* Absolute and convective instabilities of natural convection flow in boundary-layer regime. *Phys. Rev.* E **70**, 066311.

Tao, J., LeQuéré, P. & Xin, S. 2004*b* Spatio-temporal instability of the natural-convection boundary layer in thermally stratified medium. *J. Fluid Mech.* **518**, 363–379.

Trefethen, L.N. 2008 Is Gauss quadrature better than Clenshaw–Curtis? *SIAM Rev.* **50**, 67–87.

Watson, J. 1960 On the non-linear mechanics of wave disturbances in stable and unstable flows Part 2. The development of a solution for plane Poiseuille flow and for plane Couette flow. *J. Fluid Mech.* **9**, 371–389.

Wu, X. & Zhang, J. 2008 Instability of a stratified boundary layer and its coupling with internal gravity waves. Part 1. Linear and nonlinear instabilities. *J. Fluid Mech.* **595**, 379–408.

XIAO, Y., ZHANG, B., ZHAO, M. & WANG, S. 2022 Instabilities of buoyancy-induced flow along vertical cylinder in thermally stratified medium. *Phys. Fluids* **34**, 044109.

XIONG, X. & TAO, J. 2017 Lower bound for transient growth of inclined buoyancy layer. *Z. Angew. Math. Mech.* **38**, 779–796.